

# Title here

ELIO CAMPITELLI \* AND LEANDRO DÍAZ

CIMA UBA blablabla

CAROLINA VERA

## ABSTRACT

Enter the text of your abstract here. This is a sample American Meteorological Society (AMS) L<sup>A</sup>T<sub>E</sub>X template. This document provides authors with instructions on the use of the AMS L<sup>A</sup>T<sub>E</sub>X template. Authors should refer to the file `amspaper.tex` to review the actual L<sup>A</sup>T<sub>E</sub>X code used to create this document. The `template.tex` file should be modified by authors for their own manuscript.

*Significance statement.* This is significant because I wrote it.

## 1. Introduction

yada yada SAM yada yada circulation.. yada yada so important. yada yada many impacts.

Fogt et al. (2012) studied the characteristics of the asymmetric structure of the SAM. It computed the zonally anomalous component of mean sea level pressure (MSLP) composites for positive and negative SAM events and created two indices by projecting MSLP fields onto them. However, the use of composites leads to some issues that affects the interpretability of the results. First, they can be dependent on the choice of threshold used to define positive and negative events. Secondly, by discarding data that don't meet the threshold, they don't use all the information available. Due to the relative short timeframe used, this leads to some composites being composed of as little as 4 years. Third, the resulting composites corresponding to each polarity and season are derived from the average of different amount of fields and from different years. This last issue is particularly important in light of the changing structure of the SAM before and after 1980 (Silvestri and Vera 2009). In Fogt et al. (2012), the DJF SAM+ composite uses only 7 years, 5 of which are later than 1988, whereas all of the 8 years used for their DJF SAM- composite are from earlier than 1988.

## 2. Methods

### 1) DATA

To describe the Southern Annular Mode and its variability we used monthly geopotential height at 2.5° longitude

by 2.5° latitude of horizontal resolution and 37 vertical isobaric levels from ERA5 (Hersbach et al. 2020) for the period 1979 to 2018. We restrict our analysis to the post-satellite era to avoid any confounding factors arising from the introduction of satellite observations.

We describe the relationship between the SAM indices and temperature and precipitation. We use temperature data from NOAA's Merged Land Ocean Global Surface Temperature Analysis V4.0.1 (Vose et al. 2012; Smith et al. 2008), which blends land and ocean temperature analysis into a monthly global grid 5° latitude by 5° longitude. For precipitation, we use monthly, 0.5° latitude by 0.5° longitude data from the Global Precipitation Climatology Centre (Schneider et al. 2015).

### 2) DEFINITION OF INDICES

Traditionally the Southern Annular Mode (SAM) is defined as the leading Empirical Orthogonal Mode (EOF) of sea level pressure or geopotential height at lower levels (Hoskins et al. 2012). Following Baldwin and Dunkerton (2001), we extend that definition vertically and use the term SAM to refer to the leading EOF of the monthly anomalies of geopotential field south of 20°S at each level. We performed EOFs by computing the Singular Value Decomposition of the data matrix consisting in 481 rows and 4176 columns (144 points of longitude and 29 points of latitude). We weighted the values by the square root of the cosine of latitude to account for the non-equal area of each gridpoint (Chung and Nigam 1999).

To separate between the zonally symmetric and asymmetric components of the SAM, we computed the zonal mean and anomalies of the full SAM spatial pattern, as shown in Figure 1 for 700hPa. The full spatial signal ( $\text{EOF}_1(\lambda, \phi)$ ) is the sum of the zonally asymmetric ( $\text{EOF}_1^*(\lambda, \phi)$ ) and symmetric ( $[\text{EOF}_1](\lambda, \phi)$ ) components.

---

\*Corresponding author: Elio Campitelli, elio.campitelli@cima.fcen.uba.ar

We then compute the “Full”, “Asymmetric” and “Symmetric” indices, by regressing each geopotential field on the respective patterns (weighting by the cosine of latitude). The three indices are normalised by dividing them by the standard deviation of the “Full” index at each level. As a result, the magnitude between indices is comparable. However, only “Full” index will have unit standard deviation per definition.

Our method assumes linearity in the asymmetric component of the SAM. That is, we assume that zonal symmetries associated with positive SAM are opposite and equal to the ones associated with negative SAM. Fogt et al. (2012)’s composites (their Figure 4) suggest that this might not be entirely valid, although we argue that much of that apparent non-linearity is due to the heterogeneous nature of the selected years for constructing the composites. Using our data (from 1979 to 2018), seasonal composites of zonal anomalies of 700 hPa geopotential height for SAM+ (Full SAM index greater than 1 standard deviation) and SAM- (smaller than negative 1 standard deviation) show relatively high pattern correlations all seasons and are visually very linear (Figure A9). Therefore, we believe that our method is at the very least a reasonable approximation of the phenomenon.

By computing a single EOF pattern using data for all months we are assuming that the zonal anomalies of the SAM are the same in all seasons. Geopotential zonal anomalies computed by projecting the first EOF of *each season* are very similar to each other (Figure A10) and show pattern correlations between 0.65 (DJF with JJA) and 0.9 (between MAM and SON). Based on this, we believe that our initial assumption is not unreasonable.

Finally, we assume that the zonally asymmetric pattern is stationary in time. Silvestri and Vera (2009) suggest that this might not be the case between 1958 and 2004 but the period we analyse is much shorter (1979-2018) so it’s unlikely that we could observe significant changes. Moreover, zonal asymmetry of the spatial patterns for the two halves of the period (1979 to 1998 and 1999 to 2018) show no systematic change (Figure A11).

### 3) REGRESSIONS

We perform linear regression to quantify the association between the SAM indices and other variables. Since the Asymmetric and Symmetric SAM indices are significantly correlated with each other, to capture the variability explained uniquely by each index we use one multiple linear regression instead of two simple linear regressions. To obtain the linear coefficients of a variable  $X$  (geopotential, temperature, precipitation, etc. . . ) with the Asymmetric SAM ( $SAM_a$ ) and Symmetric SAM ( $SAM_s$ ) we fit the equation

$$X(\lambda, \phi, t) = \alpha(\lambda, \phi) SAM_a + \beta(\lambda, \phi) SAM_s + X_0(\lambda, \phi) + \epsilon(\lambda, \phi, t)$$

where  $\lambda$  and  $\phi$  are the longitude and latitude,  $t$  is the time,  $\alpha$  and  $\beta$  are the linear coefficients,  $X_0$  and  $\epsilon$  are the constant and error terms. From this equation,  $\alpha$  represents the (linear) association of  $X$  with the variability of the Asymmetric SAM that is not explained by the variability of the Symmetric SAM; in other words, it is proportional to the partial correlation of  $X$  and the Asymmetric SAM, controlling for the effect of the Symmetric SAM and viceversa for  $\beta$ .

At 2.5° by 2.5° resolution, a single regression field is composed of thousands of regressions. In such case, using naive p-values to test for significance leads to misleading results (Walker 1914; Katz and Brown 1991). While there are multiple proposed solutions in the literature, Wilks (2016) suggests that adjusting p-values by controlling for the False Discovery Rate (Benjamini and Hochberg 1995) is a simple and effective method to ameliorate this issue. Therefore, p-values showed in regression fields are all adjusted following Benjamini and Hochberg (1995).

When performing a separate regression for each trimester (DJF, MAM, JJA, SON) we first average the relevant variables to obtain a single value for each year and each trimester.

## 3. Results

### a. Temporal evolution

The temporal evolution of the Asymmetric and Symmetric SAM was firstly assessed. Figure 2 shows the corresponding time series for 700 hPa and 50 hPa and their corresponding density estimates. We selected these two levels as representative of the tropospheric and stratospheric variability respectively. As will be shown later, both indices are highly coherent within each atmospheric layer, therefore is reasonable to take one level as representative of each layer.

Month-to-month variability is evident for both indices, with noisy variations in the low frequency. At first glance the series can be distinguished by their distributions. Compared to the stratospheric indices, the tropospheric indices are much more long-tailed; that is, extreme values (both negative and positive) abound. The Asymmetric series have both more variability in the higher frequencies than the Symmetric series.

The stratospheric Symmetric SAM varies strongly with a two-year period, which can be seen by spectral analysis (Figure A3). This might suggest a link between stratospheric SAM variability and QBO. There is a local peak at 2 years in the periodogram of the tropospheric Symmetric SAM also, although it’s not statistically significant. In the troposphere the most significant peak of variability is found in the Asymmetric index at around 3.6 months.

From Figure 2 we can see that the Asymmetric and Symmetric time series appear to be correlated. Moreover, looking at the extremes in the stratosphere, the Symmetric series

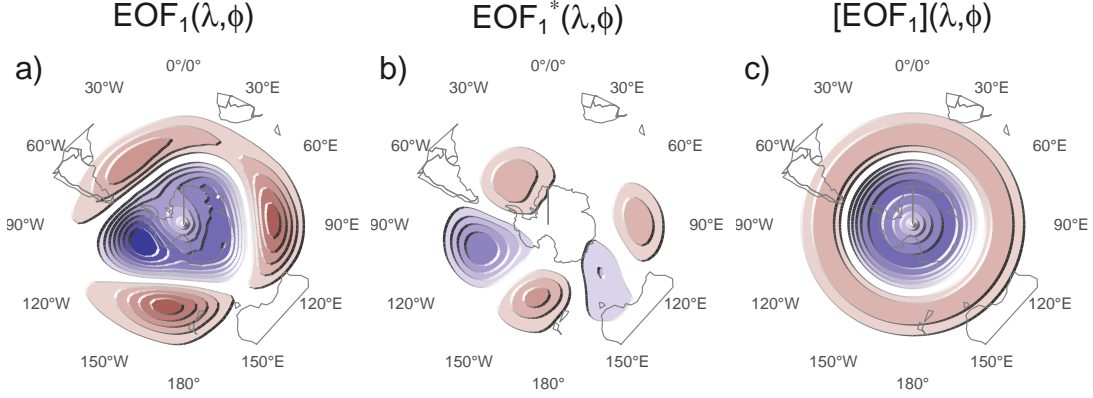


FIG. 1: Spatial patterns of the first EOF of 700 hPa geopotential height. Full field (left), zonally asymmetric component (middle) and zonally symmetric component (right). Arbitrary units.

fig:method

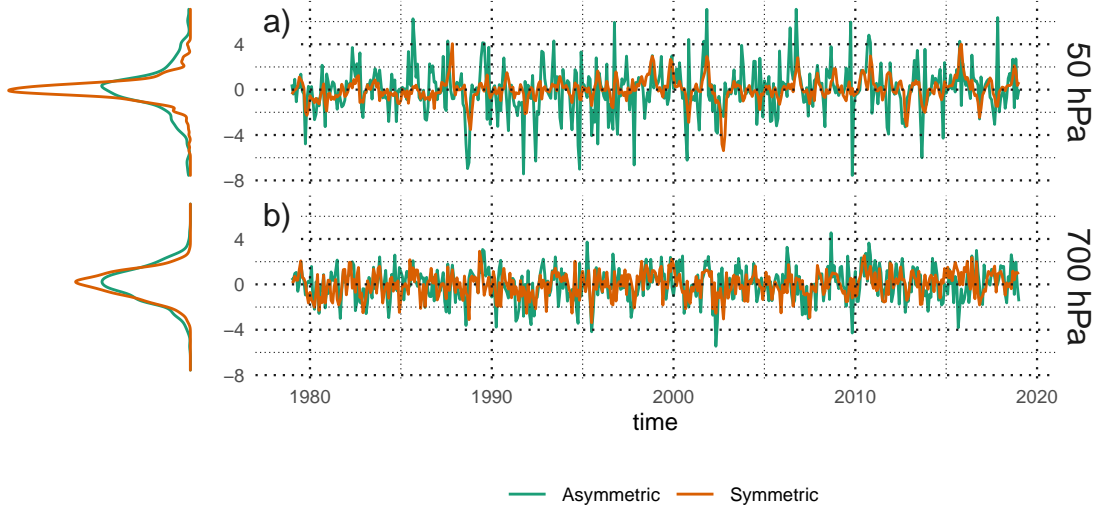


FIG. 2: Time series for the asymmetric SAM and symmetric SAM and density estimates.

fig:asysam-timeseries

appears to lag the Asymmetric series (see, for example, the positive events on late 1987). We show these correlations, across all the levels of the reanalysis for zero and -1 lag (Asymmetric index leading the Symmetric index), in Figure 3. Zero-lag correlations between the Asymmetric and Symmetric series are relatively constant throughout the troposphere, fluctuating between 0.39 and 0.45. One-month-lag correlations are similarly constant but significantly reduced to around 0.17. In the stratosphere, zero-lag correlations drop to a minimum of 0.21 at 20 hPa and then it increases again monotonically with height up to the uppermost level of the reanalysis (although results near the top of the mod-

els are to be interpreted with care). At the same time, one-month-lag correlations increase with height. As a consequence, stratospheric Asymmetric index tend to precede corresponding Symmetric index.

Figure 4a shows (zero-lag) cross-correlation across levels for the Full, Symmetric and Asymmetric SAM indices. For the Full SAM (panel a), high values below 100 hPa reflect the vertical (zero-lag) coherency throughout the troposphere. Above 100 hPa correlation between levels falls off more rapidly, indicating less coherent (zero-lag) variability. Therefore, there is a non negligible correlation between the troposphere and the lower-to-middle stratosphere. Ex-

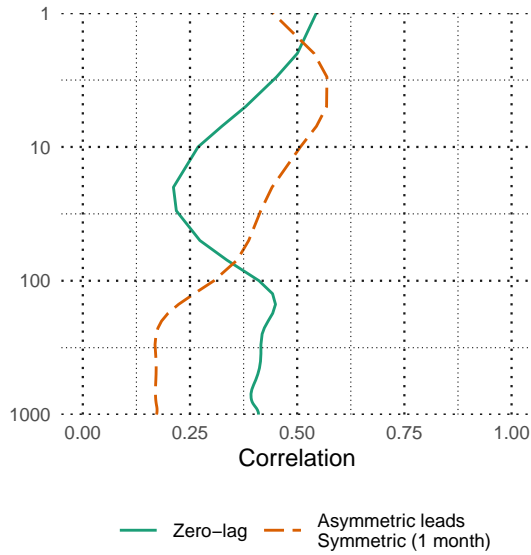


FIG. 3: Correlation between the Symmetric and Asymmetric SAM at each level for lag zero and lag -1 (Asymmetric leads Symmetric).

fig:cor-lev

Examining panels b and c, we see that the Asymmetric and Symmetric SAM share the same high level of coherency in the troposphere but they differ in their stratospheric behaviour. Stratospheric coherency is stronger for the Asymmetric SAM than the Symmetric SAM. The stratospheric Symmetric SAM seems to connect more strongly to the troposphere than the Asymmetric SAM.

The trends for each of the indices (Full, Symmetric, Asymmetric) were evaluated for the whole period 1979-2018 at each level (Figure 5) for the whole year and separated by trimesters. The Full SAM index presents a statistically significant trend (panel a.1) that extends throughout the troposphere up to about 50 hPa and reaches its maximum value at 100 hPa. The seasonal trends (rest of column a) indicate that positive trends are present in Autumn and particularly in Summer, where the 100 hPa maximum is much more defined. Positive trends have been documented by previous studies (e.g. Fogt and Marshall 2020, and references therein) using indices of the SAM based on surface or near-surface circulation.

By separating the SAM signal in its Asymmetric and Symmetric parts, we can not only see that these trends are almost entirely due to the Symmetric component (column b vs. column c), but in some cases the trends become more clear. In Summer, the Asymmetric SAM has a statistically non significant negative trend in the middle troposphere that obscures the trend in the Full index; as a result, trends computed using only the Symmetric component are more clear (compare the shading region in panel a.2 and c.2). In Autumn, using the Symmetric SAM reveals a statistically

significant positive trend in the stratosphere that is not significant using the Full index.

We stress that these are only linear trends during the whole period and the absence of a statistically significant signal should not be taken as evidence of no systematic change. In particular, going back to Figure 2, we can see an evident change in the stratospheric Asymmetric component (red line in panel a) between the 90's, when we see a dominance of extreme negative values, and the 00's, when we see the inverse. This change is restricted to the Winter months: the linear trend for JJA starting in 1990 for the Asymmetric component at 50hPa is  $0.37 \pm 0.22$ .

Figure 6 shows decadal trends for the explained variance of each index. There is no evidence of a significant trend in the stratosphere. In the troposphere, there is a positive trend for the Asymmetric SAM and no significant trend for the Symmetric SAM. This suggests that the SAM has become more asymmetric in the period from 1979 to 2018. The change is slight, though; of the order of 1% increased explained variance per decade.

### b. Spatial patterns

To show if, and to what extent, the Asymmetric and Symmetric SAM indices indeed capture the asymmetric and symmetric component of the SAM respectively, we computed the spatial regression of geopotential height anomalies on these indices and the Full SAM index. Figure 7 shows these regressions. Regression coefficients in column a are computed using the Full SAM. Regression coefficients in columns b and c are computed using multiple regression using the Asymmetric and Symmetric indices at the same time. Thus, they are to be interpreted as the patterns associated with each index, removing the variability (linearly) explained by the other index.

In the stratosphere, the spatial pattern associated with the Full SAM is more clearly dominated by a zonally symmetric, monopolar structure (panel a.1) which is, however, not perfectly centered in the South Pole. The monopole obtained by multiple regression with the Asymmetric and Symmetric SAM (panel c.1) is much more symmetric and the shift from total symmetry is captured by the regression pattern of the Asymmetric SAM as a wave-1 with maximum anomalies above the Belinghausen Sea on the Western Hemisphere and the Davis Sea in the Eastern Hemisphere (panel b.1).

In the troposphere, panel a.2 shows the well known combination of zonally symmetrical annular mode with zonal asymmetries in the form of a wave-3. The regression using the Asymmetric and Symmetric SAM indices successfully disentangle both structures. The Asymmetric component gives rise to a cleaner zonal wave (panel b.2) and the Symmetric component is associated with a truly annular mode, almost devoid of zonal asymmetries (panel c.2). The wave-3 pattern observed in panel b.2 is rotated

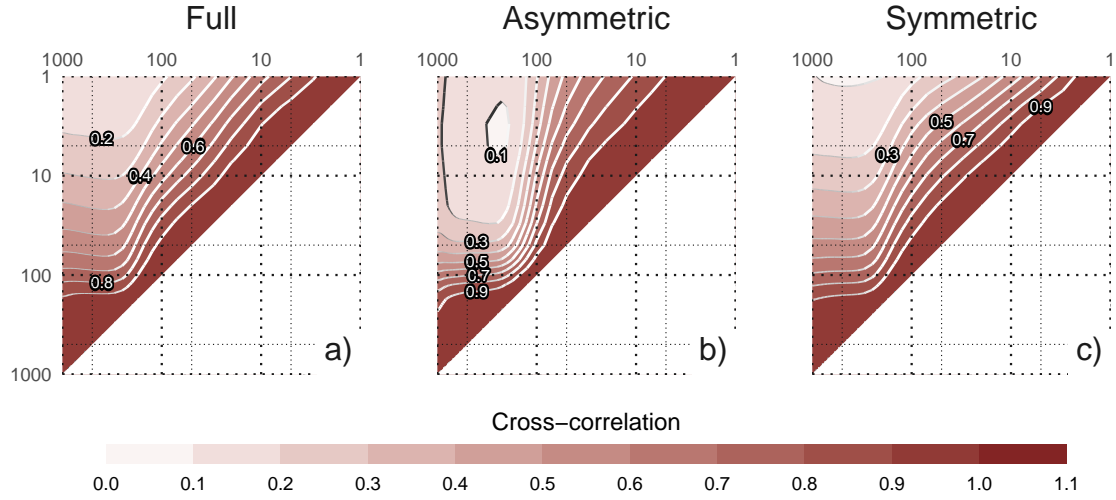


FIG. 4: Cross correlation between levels of the Full, Asymmetric and Symmetric SAM.  
fig:cross-correlation

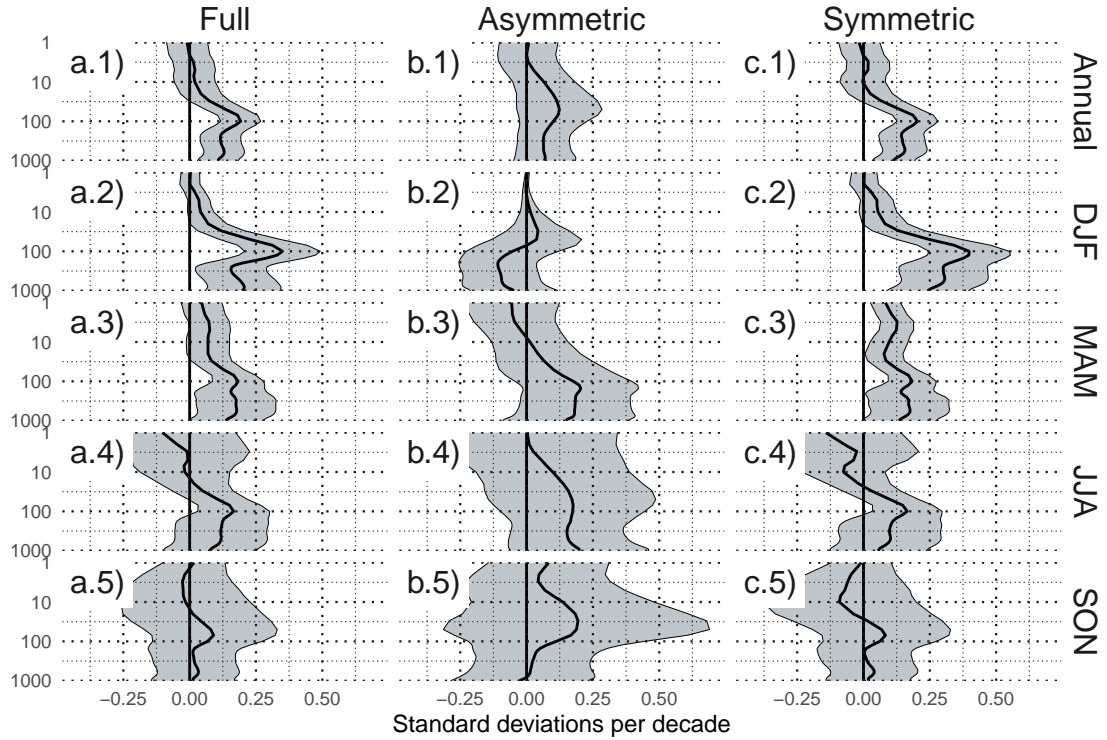


FIG. 5: Decadal normalised trends for each index at each level for annual (row a) and seasonal values (rows b-e) for the period 1979-2018. Shading indicates the 95% confidence interval.  
fig:trends

by half a wavelength from the average position of the mean dex, whose reference locations are marked with points in wave-3 pattern associated with Raphael (2004)'s ZW3 in the figure. Thus, the tropospheric Asymmetric SAM in-

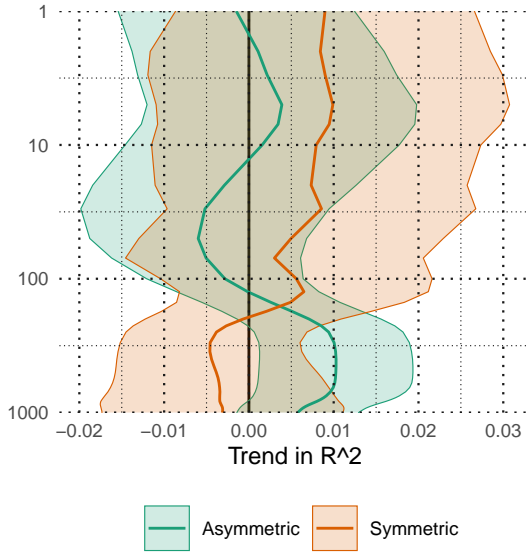


FIG. 6: Decadal trends for explained variance of each index at each level for the period 1979-2018. Shading indicates the 95% confidence interval.

fig:r-squared-trend

dex represents a zonal displacement in the position of the climatological wave-3 pattern.

The amplitude of first zonal wave numbers at each latitude at 50 hPa and 700 hPa is shown in Figure 8, where wave number zero represents the amplitude of the zonal mean. Column b shows that the Asymmetric SAM is overwhelmingly dominated by wave 1 in the stratosphere (panel b), while in the troposphere it is composed of zonal waves 3 to 1 in decreasing level of importance (panel b). Looking at panel b.2 from Figure 7, it becomes apparent that zonal waves 1 and 2 modulate the amplitude of zonal wave 3, which –as mentioned before– is larger in the Western Hemisphere than in the Eastern Hemisphere.

To analyse the vertical structure of the geopotential anomalies associated with the asymmetric SAM index, we show a vertical cross section of regressions of mean geopotential height between 65°S and 40°S for the 50 hPa Asymmetric SAM index (panel a) and for the 700 hPa Asymmetric SAM index (panel b) (Figure 9). The geopotential anomalies associated with the stratospheric Asymmetric SAM (panel a) are clearly constrained to the stratosphere, which underscores the uncoupling between the stratospheric and tropospheric Asymmetric SAM. The vertical structure of this signal tilts about 60° to the West between 100 hPa and 1 hPa, suggesting baroclinic processes. Interestingly, the signal in the stratosphere maximises near 10 hPa despite using the 50 hPa index for the regression.

The tropospheric Asymmetric SAM (panel b) has significant signals that extend upwards to the uppermost levels of the reanalysis. In the troposphere, the wave-3 structure is

equivalent barotropic with maximum amplitude at roughly 250 hPa. The anomalies are much more intense in the Western hemisphere, where they extend into the stratosphere. In the Eastern hemisphere the wave-3 signal is weaker and confined to the troposphere while negative anomalies dominate in the stratosphere. So, while the tropospheric Asymmetric SAM index is associated with stratospheric geopotential anomalies, these do not project strongly onto the stratospheric Asymmetric SAM.

The structures shown in panels a and b in Figure 9 are surprisingly robust to the choice of index level. For any stratospheric (above 100 hPa) index, the resulting anomalies are very similar to the wave-1 structure with maximum near 10 hPa in panel a. Conversely, for any tropospheric (below 100 hPa) index, the result is very similar to panel b. The patterns mainly change in amplitude.

The wave-3 pattern from Figure 7 panel b.2 is very similar to the Pacific-South American Pattern (Mo and Ghil 1987; Kidson 1988) which is a teleconnection pattern associated with the ENSO (Karoly 1989). Indeed, Fogt et al. (2011) showed that there is a significant relationship between the SAM and the ENSO. The correlation between the full SAM and the ENSO as measured by the Oceanic Niño Index (Bamston et al. 1997) (ONI) is -0.16. This relationship is captured entirely by the Asymmetric SAM, as this index has a partial correlation of -0.26 with the ONI controlling for the effect of the Symmetric SAM, whereas the Symmetric SAM's partial correlation with the ONI is essentially null (0.019). We performed the same analysis using the Multivariate ENSO Index (Wolter and Timlin 2011) and the Southern Oscillation Index (Ropelewski and Jones 1987) to conclude that these results do not depend on the ENSO index used.

### c. Impacts

The SAM has been shown to be associated with important surface variables such as temperature and precipitation (e.g. Gillett et al. 2006, and see Fogt and Marshall (2020) for a review). Naturally, most studies on the surface impacts of the SAM are based on an index identical or analogous to what we call Full SAM index (Fogt et al. (2012) being the only exception that we are aware of). We regress surface temperature and precipitation onto each of the three SAM indices to see if there are different surface impact associated with the asymmetric and symmetric SAM circulation.

Figure 10 shows regression coefficients of each index at 700 hPa with surface temperature for each trimester. In Summer positive values of the Full SAM index (panel a.1) are associated with negative temperature anomalies near Antarctica which are surrounded by a ring of positive anomalies. The ring is not zonally symmetric, as there are three clear local maximums around 30°W, 15°E and 50°E and a local minimum (with negative sign) around



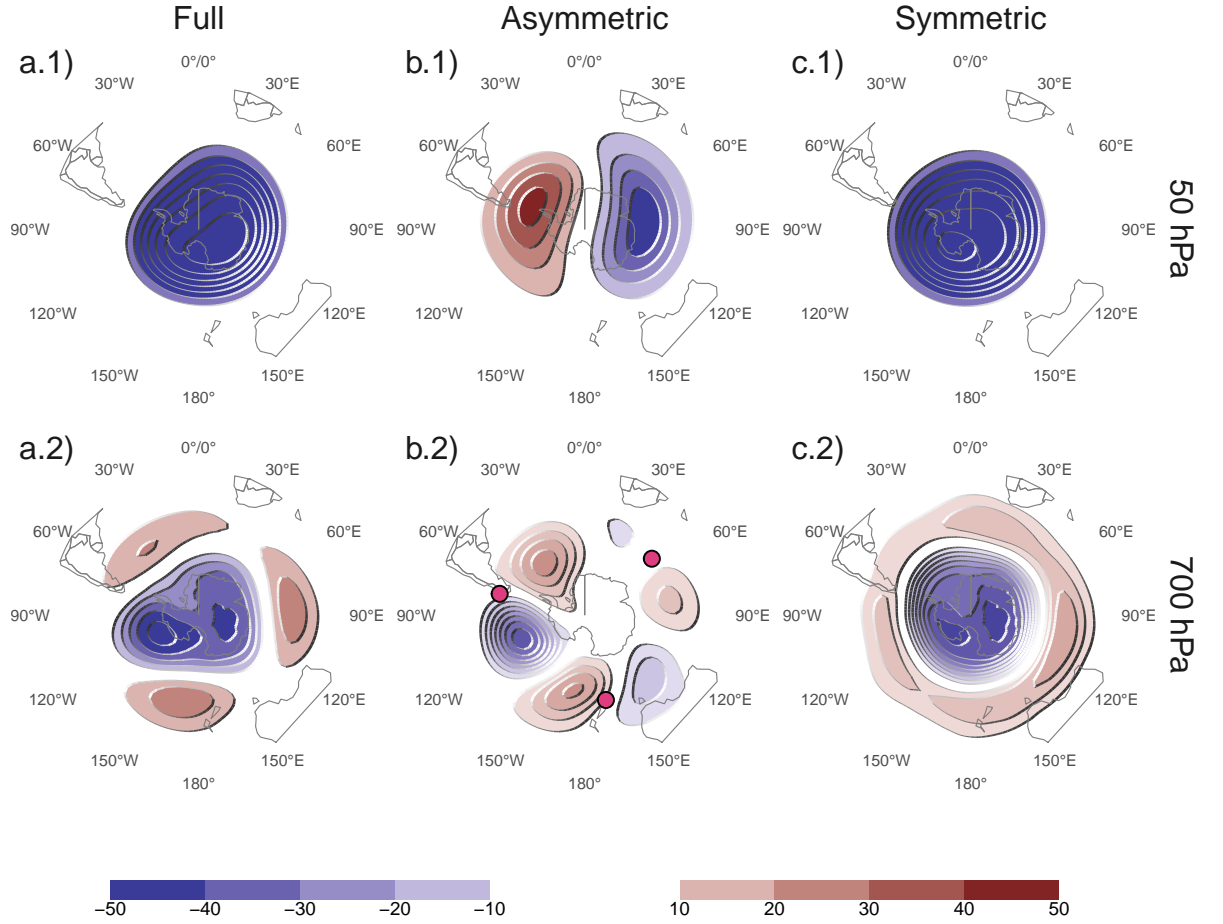


FIG. 7: Regression patterns of geopotential height at 30, 300 and 700 hPa with the Full, Asymmetric and Symmetric SAM. The regression patterns for Asymmetric and Symmetric SAM are the result of one multiple regression using both indices, not of two simple regressions involving each index by itself. Points marked on panel b.2 are the location of the reference points used by Raphael (2004) for their Zonal Wave 3 index.  
fig:2d-regr

120°W. In the tropics, there are negative anomalies in the equatorial Pacific, consistent with the negative correlation between SAM and ENSO. Panels b.1 and c.1 show temperature anomalies associated with positive values of the Asymmetric and Symmetric SAM, respectively. Both the local maximums in the ring and the anomalies in the Pacific regions are present mostly on the Asymmetric SAM regression map, while temperature patterns linked to positive Symmetric SAM show a more zonally consistent ring and less relation to the tropics. Noticeable, temperature anomalies in the Indian ocean, South Africa and Australia are strongly related to positive values of Asymmetric SAM. This signal is not present in the regression pattern with the Full SAM. Spring (row 4) features very similar patterns but of generally smaller in magnitude and statistical significance.

In Autumn and Winter (rows 2 and 3) the positive ring is only present through its local maximums in the regression with the Full SAM. There are also negative anomalies in Southern Australia, and positive anomalies over New Zealand and Southern South America. These patterns are not significant in the sense that there are no areas with p-values below 0.05 when controlling for FDR following Wilks (2016). However, repeating this analysis with 2-meter temperature from ERA5 resulted in similar patterns that were statistically significant. Moreover, similar features were observed in station measurements by Jones et al. (2019), although using data from 1957 to 2016.

The pattern of negative anomalies in the pole surrounded by positive anomalies roughly seen in all seasons—although with varying intensity and small-scale details—is consistent with the intensification and poleward migration of

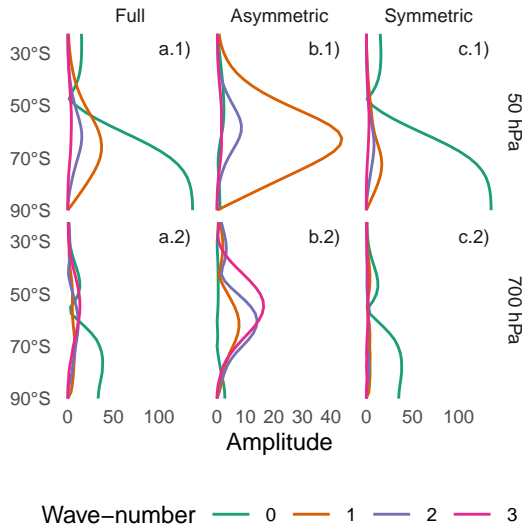


FIG. 8: Planetary wave amplitude for the regression patterns at 50 and 700 hPa. Note the varying x axis.  
fig:wave-amplitude

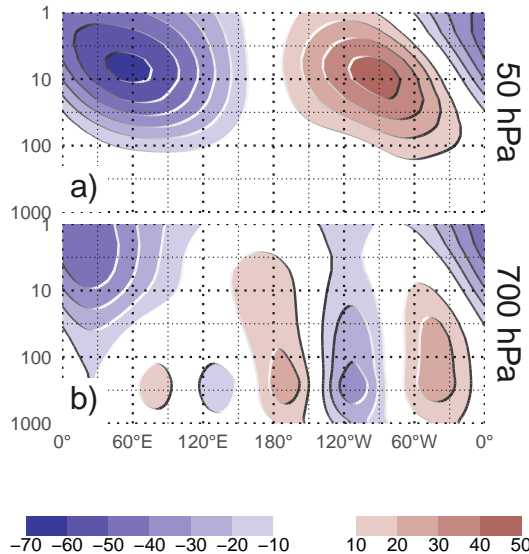


FIG. 9: Asymmetric coefficient of the multiple regression of mean monthly geopotential height anomalies between 65 and 40 South. (#FIXME this caption needs some love)  
fig:vertical-regression

the westerlies commonly linked to the SAM. It's then not surprising to see it more clearly in association with the Symmetric SAM (at least in Summer and Spring).

These results suggests that Asymmetric and Symmetric SAM indices are associated with overall distinct temperature patterns which may not be apparent when using the Full SAM index.

Figure 10 column b can be partially compared with Figure 11 from Fogt et al. (2012). Although they used station data from 1958 to 2001, a lot of the characteristics are reproduced here, such as the strong signal in New Zealand and Australia in Summer and Spring.

Regression of the SAM indices with seasonal mean precipitation and 700 hPa geopotential height are shown Figures 11 and 12 for Australasia and South America respectively. South Africa is not shown because no significant signal was detected there.

In Australia, the annual regression shows that the Full SAM index is positively associated with precipitation in the Southeastern region (Figure 11 panel a.1), which reproduces the results from Gillett et al. (2006). The separation between Asymmetric and Symmetric SAM suggest that this positive anomaly is explained by the Symmetric SAM only in the East coast (panel c.1). Geopotential anomalies associated with this index (black contours) are indicative of easterly flow from the Tasman Sea, which could explain the positive anomalies in precipitation as found by Hendon et al. (2007). The Asymmetric SAM appears related to increased precipitation in the West coast of Southeastern Australia (panel b.2), which could similarly be explained by the anomalous westerly circulation transporting moist air to the continent from the Indian Ocean.

This Spring signal is broadly consistent with Hendon et al. (2007), but whereas Hendon et al. (2007) also detected a strong signal in Summer, panel a.2 shows no statistically significant association (although the coefficients have the consistent sign).

The seasonal-level regressions show statistically significant anomalies only in Spring, when positive Full SAM is associated with positive precipitation anomalies in Eastern Australia (panel a.5). In this trimester the Symmetric SAM seems to be associated with precipitation in a relatively reduced area of the East Coast (panel c.5) while the positive precipitation anomalies related with positive Asymmetric SAM affect all Eastern Australia (panel b.5).

In Summer, positive Full SAM index is associated with positive precipitation anomalies in Western and Eastern Australia, particularly in the North East (panel a.2). The Eastern part being dominated by the relationship with the Symmetric SAM and the Western, by the Asymmetric SAM. In Autumn, the regression with Full SAM shows positive values in the North, similar to Summer, and a broad area of positive values in the North-East to South-West direction. This structure seems to be associated with the Symmetric SAM, while the Northern positive values are associated with the Asymmetric SAM. In Winter we see the same NE to SW aligned anomaly (although with much reduced amplitude) that is also present only in relation with the Symmetric SAM. None of these regression coefficients are statistically significant at the 95% level.

In South America (Figure 12), the annual-level regression shows that the SAM is associated with statistically



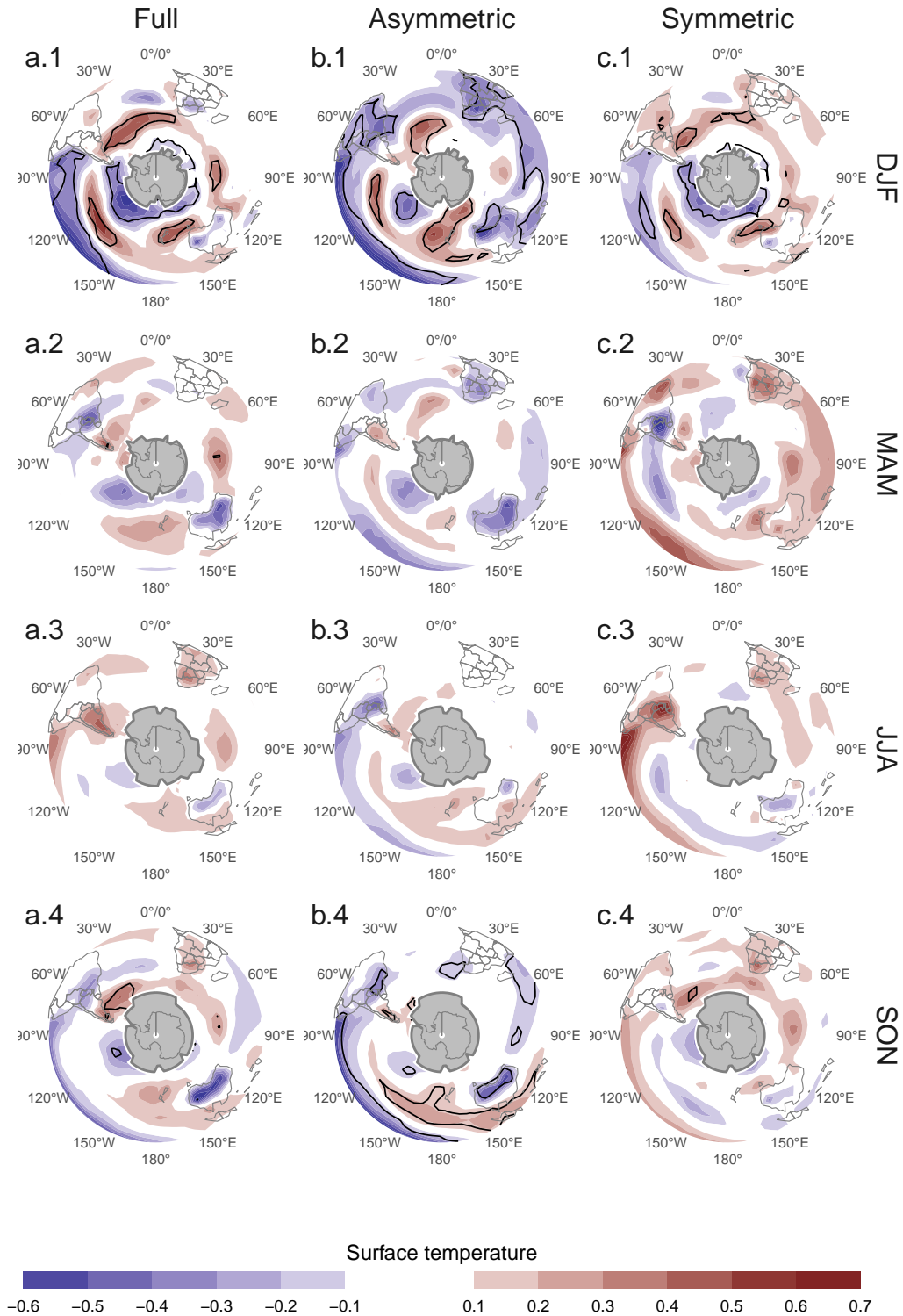


FIG. 10: Regression pattern of surface temperature with Asymmetric and Symmetric SAM. P-values smaller than 0.05 (controlling for False Detection Rate) as hatched areas. Gray areas have more than 15% of missing data.  
fig:regr-air-season

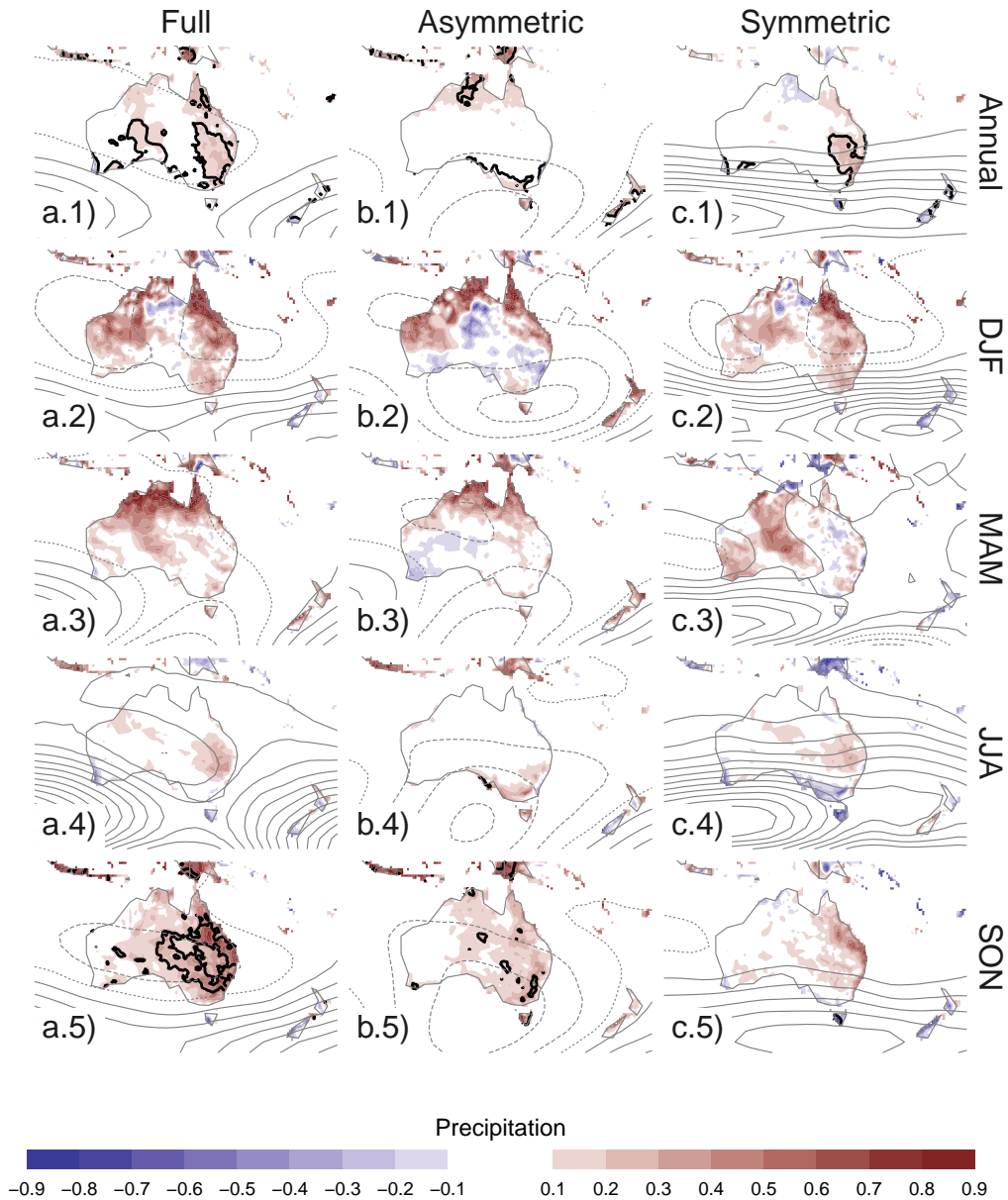


FIG. 11: Regression pattern of precipitation with Asymmetric and Symmetric SAM. P-values smaller than 0.05 (controlling for False Detection Rate) as hatched areas.

fig:pp-regr-oceania

significant precipitation decrease in Southeastern South America (SESA) and Southern Chile and non-significant increase in South Brazil, near the South Atlantic Convergence Zone (SACZ) (panel a.1). Panels b.1 and c.1 show a remarkably clean separation between the Asymmetric SAM –associated with the Southeastern South American and Southern Brazilian signals– and the Symmetric SAM –associated with the signal in Southern Chile.

Except Winter, seasonal-level regressions mirror this same pattern. Even if not statistically significant, they all show negative values in Southeastern South America and Southern Chile along with positive values in Southern Brazil in relation with the Full SAM. The separation of these features between the Asymmetric SAM and Symmetric SAM regression maps is also rather consistent.

The anomalous circulation at 700 hPa associated with the Symmetric SAM (panel c.1) indicate anomalous East-

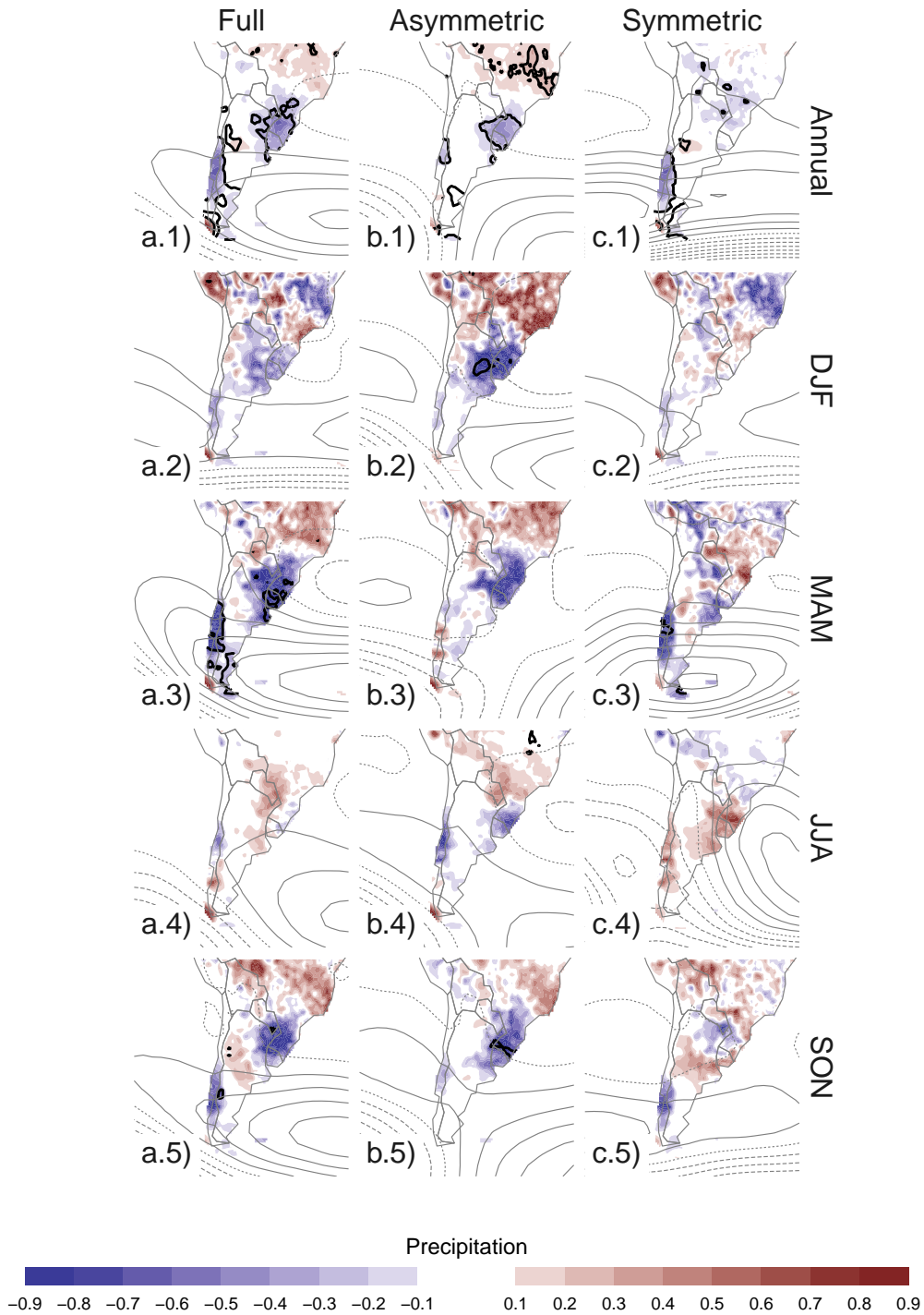


FIG. 12: Same but for america  
fig:pp-regr-america

erly flow over Southern Chile. This leads to reduced influx of moist air from the Pacific Ocean which, is the main source of precipitable water in that region. On the other

hand, the anomalous circulation associated with positive values of Asymmetric SAM (panel b.1) in the Atlantic is anticyclonic in the South and cyclonic in the North. This

creates anomalous South-Easterly flow over Southeastern South America, which inhibits the flow of the Low Level Jet to the region (Silvestri and Vera 2009, Zamboni et al. (2010)). This same pattern was found to be associated with increased precipitation in Southern Brazil during South Atlantic Convergence Zone events (Rosso et al. 2018).

There is a small area of increased precipitation with SAM near central Argentina which is also present in the station-based analysis by Gillett et al. (2006) and that is explained by the Asymmetric SAM.

#### *d. Conclusions*

In this study we tried to systematically characterise the variability of the zonally symmetric and zonally asymmetric structure of the SAM. By projecting monthly geopotential fields at each level with the corresponding asymmetric and symmetric pattern, we created two indices representing the zonally asymmetric and zonally symmetric contributions of the SAM respectively.

As expected, the Asymmetric SAM index correlates strongly with the Symmetric SAM index. In the troposphere, this correlation is maximum at zero lag, while in the stratosphere is maximised with the Asymmetric SAM leading the Symmetric SAM by one month. Since most indices of the SAM are calculated using surface or near-surface conditions, this result would suggest that they might not be sensitive to the most dramatic changes in SAM variability.

The two-year periodicty we found in the stratospheric Symmetric SAM might point to a link between the SAM and the Quasi Biennial Oscillation. There is evidence of influence between the QBO and the Northern Annular Mode (e.g. Holton and Tan 1980, Watson and Gray (2014), Zhang et al. (2020)), so it's not unlikely that the SAM would be similarly connected. However establishing this link would require further research.

As documented by previous studies, such as Fogt and Marshall (2020) (and references therein), we observe a positive trend towards positive SAM in Summer and Autumn. We show that these trends are maximised at the 100 hPa level and are explained by the zonally symmetric component. We also find a statistically significant positive trend in the Symmetric component of the SAM in the stratosphere that is not apparent in the Full SAM index. In contrast to Fogt et al. (2012) we find some evidence of the SAM becoming more zonally asymmetric, as there is a slight positive trend in the variance explained by the Asymmetric SAM explains an increasingly proportion of the total variance.

In the troposphere, the spatial patterns of geopotential associated with the Symmetric SAM is much closer to being truly annular than the patterns associated with the Full SAM index. The Asymmetric SAM, on the other hand, describes a wave-3 pattern with maximum amplitude in the

Pacific region and whose phase is rotated a quarter wavelength from the mean zonal wave 3 described by Raphael (2004)'s index. This pattern extends in the troposphere but its maximum is located at 250 hPa, which also could suggest that surface-based indices are not optimum for capturing this variability.

This wave-3 pattern is similar to the Pacific-South American Pattern, which is a teleconnection pattern linked to ENSO variability. We found that the significant correlation that exists between the Full SAM index and the Oceanic Niño Index is captured entirely by the Asymmetric SAM index. This suggests that ENSO is linked to SAM exclusively through the variability in the latter's Asymmetric component.

Temperature anomalies associated with the Full SAM broadly show a pattern of negative anomalies at polar latitudes surrounded by positive anomalies, but with many deviations from symmetry. The Asymmetric SAM index explains a big portion of these deviations. In particular, the positive phase of the Asymmetric SAM is associated with colder temperatures over Southern Brazil, South Africa and Southern Australia, as well as the negative anomalies in the equatorial Pacific consistent with the ENSO-SAM relationship delineated above. These are particularly clear in the DJF and SON trimesters, which include the months in which the ENSO teleconnection is more active (Fogt et al. (2011), Cai et al. (2020)).

In Australia the Full SAM is associated with positive precipitation anomalies in South East and this is explained by the Symmetric SAM. However, the Asymmetric SAM is associated with a small area of positive precipitation anomalies in the Eastern Coast of West Australia, maybe due to advection of moist air from the Indian Ocean.

In South America, precipitation anomalies associated with the Full SAM are negative both in Southern Chile and Southeastern South America, and positive in Southern Brazil. This features are cleanly separated between the Asymmetric and Symmetric components. The Symmetric SAM explains the negative anomalies in Southern Chile and the Asymmetric SAM, the negative-positive dipole between Southeastern South America and Southern Brazil. Individual seasons mostly follow this pattern.

Silvestri and Vera (2009) suggests that precipitation impacts linked to the SAM changed rather dramatically before and after 1980. In particular, the negative relationship with precipitation in South America was absent in some areas and switched sign in other in the earlier period. The correlation between ENSO and SAM is similarly non-stationary, also disappearing before 1973.

Seeing as both the ENSO-SAM relationship and most of the precipitation impacts in South America are captured by the Asymmetric SAM, the results presented here are most likely period-dependent. Therefore, is very likely that if we were to repeat this analysis using pre-satellite data, the resulting Asymmetric SAM would look very different.

**Acknowledgments.** NOAA Global Surface Temperature (NOAAGlobalTemp) data provided by the NOAA/OAR/ESRL PSL, Boulder, Colorado, USA, from their Web site at <https://psl.noaa.gov/>

## References

- Baldwin, M. P., and T. J. Dunkerton, 2001: Stratospheric Harbingers of Anomalous Weather Regimes. *Science*, **294** (5542), 581–584, doi:10.1126/science.1063315.
- Bamston, A. G., M. Chelliah, and S. B. Goldenberg, 1997: Documentation of a highly ENSO-related sst region in the equatorial pacific: Research note. *Atmosphere-Ocean*, **35** (3), 367–383, doi:10.1080/07055900.1997.9649597.
- Benjamini, Y., and Y. Hochberg, 1995: Controlling the False Discovery Rate: A Practical and Powerful Approach to Multiple Testing. *Journal of the Royal Statistical Society: Series B (Methodological)*, **57** (1), 289–300, doi:10.1111/j.2517-6161.1995.tb02031.x.
- Cai, W., and Coauthors, 2020: Climate impacts of the El Niño–Southern Oscillation on South America. *Nature Reviews Earth & Environment*, **1** (4), 215–231, doi:10.1038/s43017-020-0040-3.
- Chung, C., and S. Nigam, 1999: Weighting of geophysical data in Principal Component Analysis. *Journal of Geophysical Research: Atmospheres*, **104** (D14), 16 925–16 928, doi:10.1029/1999JD900234.
- Fogt, R. L., D. H. Bromwich, and K. M. Hines, 2011: Understanding the SAM influence on the South Pacific ENSO teleconnection. *Clim Dyn*, **36** (7), 1555–1576, doi:10.1007/s00382-010-0905-0.
- Fogt, R. L., J. M. Jones, and J. Renwick, 2012: Seasonal Zonal Asymmetries in the Southern Annular Mode and Their Impact on Regional Temperature Anomalies. *J. Climate*, **25** (18), 6253–6270, doi:10.1175/JCLI-D-11-00474.1.
- Fogt, R. L., and G. J. Marshall, 2020: The Southern Annular Mode: Variability, trends, and climate impacts across the Southern Hemisphere. *WIREs Climate Change*, **11** (4), e652, doi:10.1002/wcc.652.
- Gillett, N. P., T. D. Kell, and P. D. Jones, 2006: Regional climate impacts of the Southern Annular Mode. *Geophysical Research Letters*, **33** (23), doi:10.1029/2006GL027721.
- Hendon, H. H., D. W. J. Thompson, and M. C. Wheeler, 2007: Australian Rainfall and Surface Temperature Variations Associated with the Southern Hemisphere Annular Mode. *J. Climate*, **20** (11), 2452–2467, doi:10.1175/JCLI4134.1.
- Hersbach, H., and Coauthors, 2020: The ERA5 global reanalysis. *Quarterly Journal of the Royal Meteorological Society*, **146** (730), 1999–2049, doi:10.1002/qj.3803.
- Ho, M., A. S. Kiem, and D. C. Verdon-Kidd, 2012: The Southern Annular Mode: A comparison of indices. *Hydrology and Earth System Sciences*, **16** (3), 967–982, doi:10.5194/hess-16-967-2012.
- Holton, J. R., and H.-C. Tan, 1980: The Influence of the Equatorial Quasi-Biennial Oscillation on the Global Circulation at 50 mb. *J. Atmos. Sci.*, **37** (10), 2200–2208, doi:10.1175/1520-0469(1980)037<2200:TIOTEQ>2.0.CO;2.
- Jones, M. E., D. H. Bromwich, J. P. Nicolas, J. Carrasco, E. Plavcová, X. Zou, and S.-H. Wang, 2019: Sixty Years of Widespread Warming in the Southern Middle and High Latitudes (1957–2016). *J. Climate*, **32** (20), 6875–6898, doi:10.1175/JCLI-D-18-0565.1.
- Karoly, D. J., 1989: Southern Hemisphere Circulation Features Associated with El Niño–Southern Oscillation Events. *J. Climate*, **2** (11), 1239–1252, doi:10.1175/1520-0442(1989)002<1239:SHCFW>2.0.CO;2.
- Katz, R. W., and B. G. Brown, 1991: The problem of multiplicity in research on teleconnections. *International Journal of Climatology*, **11** (5), 505–513, doi:10.1002/joc.3370110504.
- Kidson, J. W., 1988: Interannual Variations in the Southern Hemisphere Circulation. *J. Climate*, **1** (12), 1177–1198, doi:10.1175/1520-0442(1988)001<1177:IVITSH>2.0.CO;2.
- Mo, K. C., and M. Ghil, 1987: Statistics and Dynamics of Persistent Anomalies. *J. Atmos. Sci.*, **44** (5), 877–902, doi:10.1175/1520-0469(1987)044<0877:SADOPA>2.0.CO;2.
- Raphael, M. N., 2004: A zonal wave 3 index for the Southern Hemisphere. *Geophysical Research Letters*, **31** (23), doi:10.1029/2004GL020365.
- Ropelewski, C. F., and P. D. Jones, 1987: An Extension of the Tahiti–Darwin Southern Oscillation Index. *Mon. Wea. Rev.*, **115** (9), 2161–2165, doi:10.1175/1520-0493(1987)115<2161:AEOTTS>2.0.CO;2.
- Rosso, F. V., N. T. Boiaski, S. E. T. Ferraz, and T. C. Robles, 2018: Influence of the Antarctic Oscillation on the South Atlantic Convergence Zone. *Atmosphere*, **9** (11), 431, doi:10.3390/atmos9110431.
- Schneider, U., A. Becker, P. Finger, A. Meyer-Christoffer, B. Rudolf, and M. Ziese, 2015: GPCC Full Data Reanalysis Version 7.0 at 0.5°: Monthly Land-Surface Precipitation from Rain-Gauges built on GTS-based and Historic Data: Gridded Monthly Totals. Global Precipitation Climatology Centre (GPCC) at Deutscher Wetterdienst, 20 - 270 MB per decadal gzip compressed NetCDF archive pp., doi:10.5676/DWD\_GPCC/FD\_M\_V7\_050.
- Silvestri, G., and C. Vera, 2009: Nonstationary Impacts of the Southern Annular Mode on Southern Hemisphere Climate. *J. Climate*, **22** (22), 6142–6148, doi:10.1175/2009JCLI3036.1.
- Smith, T. M., R. W. Reynolds, T. C. Peterson, and J. Lawrimore, 2008: Improvements to NOAA’s Historical Merged Land–Ocean Surface Temperature Analysis (1880–2006). *J. Climate*, **21** (10), 2283–2296, doi:10.1175/2007JCLI2100.1.
- Vose, R. S., and Coauthors, 2012: NOAA’s Merged Land–Ocean Surface Temperature Analysis. *Bull. Amer. Meteor. Soc.*, **93** (11), 1677–1685, doi:10.1175/BAMS-D-11-00241.1.
- Walker, S. G. T., 1914: *Correlation in Seasonal Variations of Weather, III: On the Criterion for the Reality of Relationships Or Periodicities*. Meteorological Office.
- Watson, P. A. G., and L. J. Gray, 2014: How Does the Quasi-Biennial Oscillation Affect the Stratospheric Polar Vortex? *J. Atmos. Sci.*, **71** (1), 391–409, doi:10.1175/JAS-D-13-096.1.
- Wilks, D. S., 2016: “The Stippling Shows Statistically Significant Grid Points”: How Research Results are Routinely Overstated and Overinterpreted, and What to Do about It. *Bull. Amer. Meteor. Soc.*, **97** (12), 2263–2273, doi:10.1175/BAMS-D-15-00267.1.
- Wolter, K., and M. S. Timlin, 2011: El Niño/Southern Oscillation behaviour since 1871 as diagnosed in an extended multivariate ENSO index (MEI.ext). *International Journal of Climatology*, **31** (7), 1074–1087, doi:10.1002/joc.2336.

Zamboni, L., C. R. Mechoso, and F. Kucharski, 2010: Relationships between Upper-Level Circulation over South America and Rainfall over Southeastern South America: A Physical Base for Seasonal Predictions. *J. Climate*, **23** (12), 3300–3315, doi:10.1175/2009JCLI3129.1.

Zhang, R., W. Tian, and T. Wang, 2020: Role of the quasi-biennial oscillation in the downward extension of stratospheric northern annular mode anomalies. *Clim Dyn*, **55** (3), 595–612, doi:10.1007/s00382-020-05285-4.

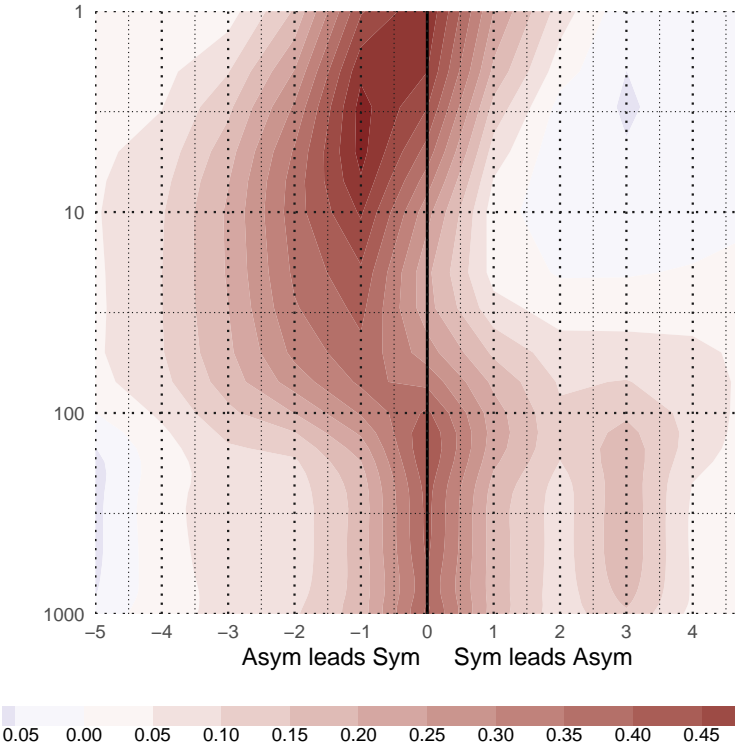


FIG. A1: Lag-correlation between Symmetric and Asymmetric SAM at each level.

fig:A1

APPENDIX

Extra figures

```
#> # A tibble: 12 x 3
#>   item1 item2 correlation
#>   <fct> <fct>      <dbl>
#> 1 MAM   DJF      -1.16e-33
#> 2 JJA   DJF       3.07e-34
#> 3 SON   DJF       2.55e-33
#> 4 DJF   MAM      -1.16e-33
#> 5 JJA   MAM       1.84e-33
#> 6 SON   MAM       1.53e-32
#> 7 DJF   JJA       3.07e-34
#> 8 MAM   JJA       1.84e-33
#> 9 SON   JJA      -4.03e-33
#> 10 DJF  SON       2.55e-33
#> 11 MAM  SON       1.53e-32
#> 12 JJA  SON      -4.03e-33
```



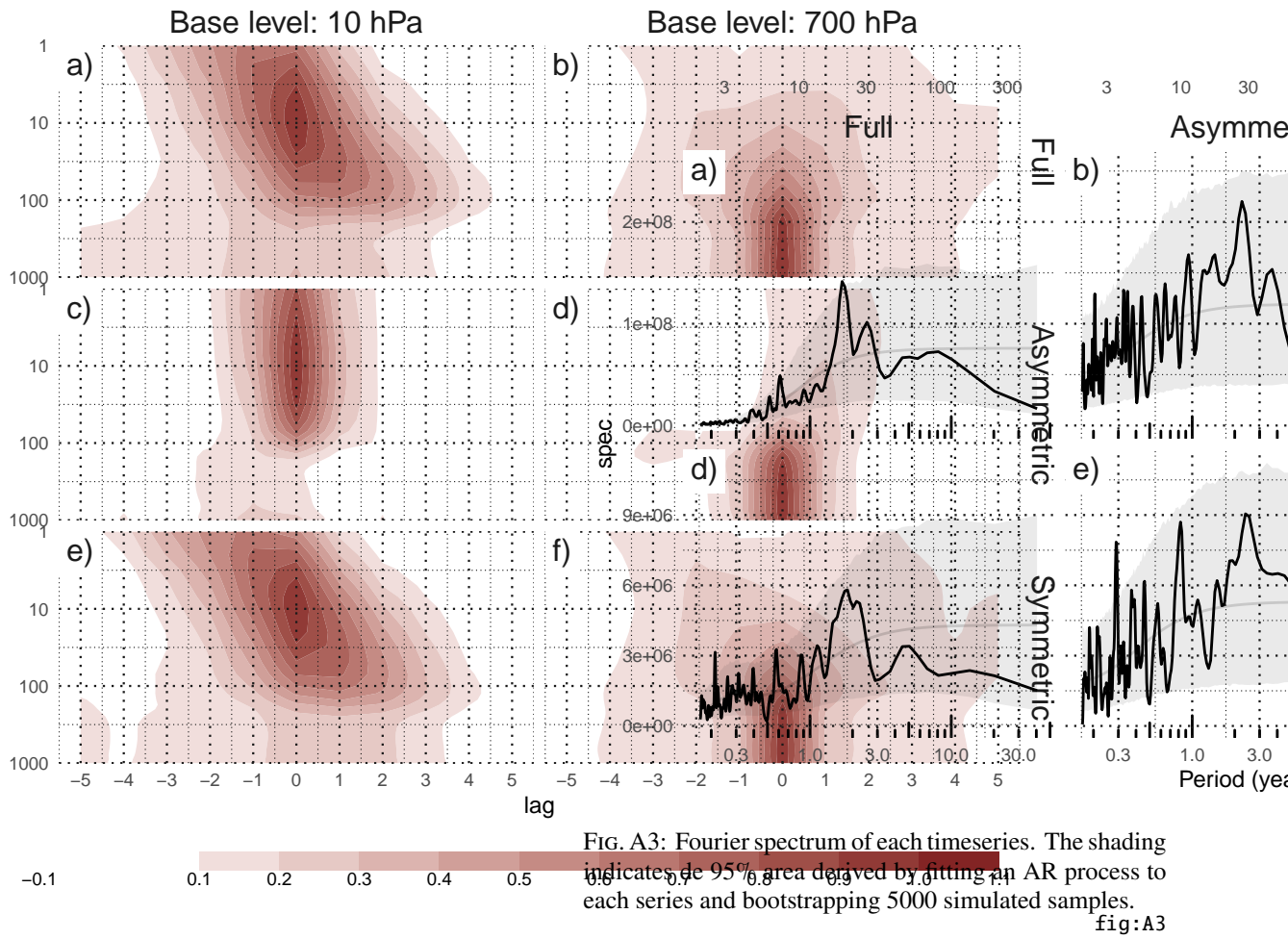


FIG. A2: Cross-correlation functions for each index and two different base levels.

fig:A2 ccf-levels

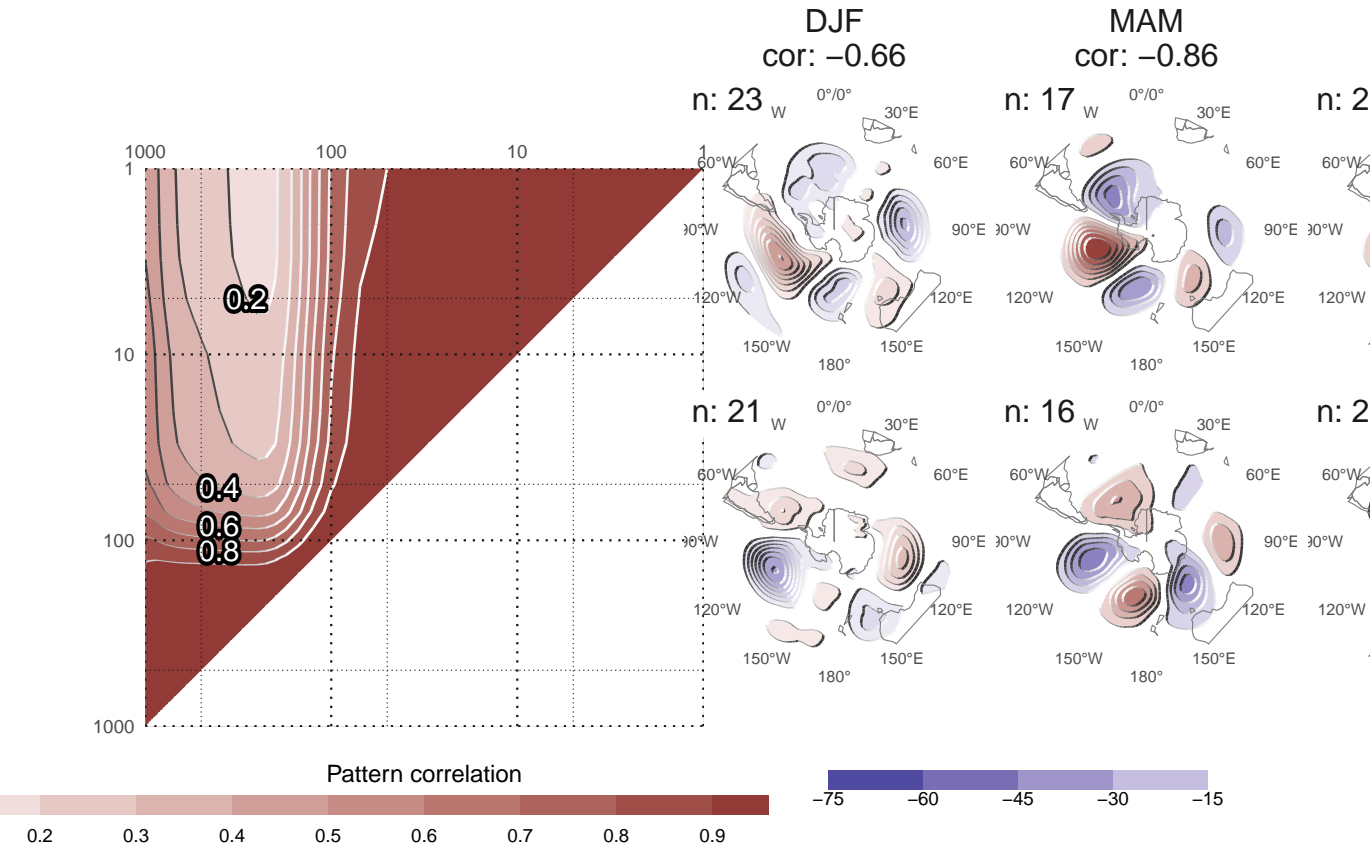


FIG. A4: Pattern cross-correlation #FIXME!

fig:A8

FIG. A5: 700 hPa Geopotential height zonal anomalies of composites of positive and negative SAM months selected using 1 standard deviation as threshold. Numbers in the column headers are pattern correlation between SAM+ and SAM- composites and number of monthly fields used to construct the composites.

fig:A9

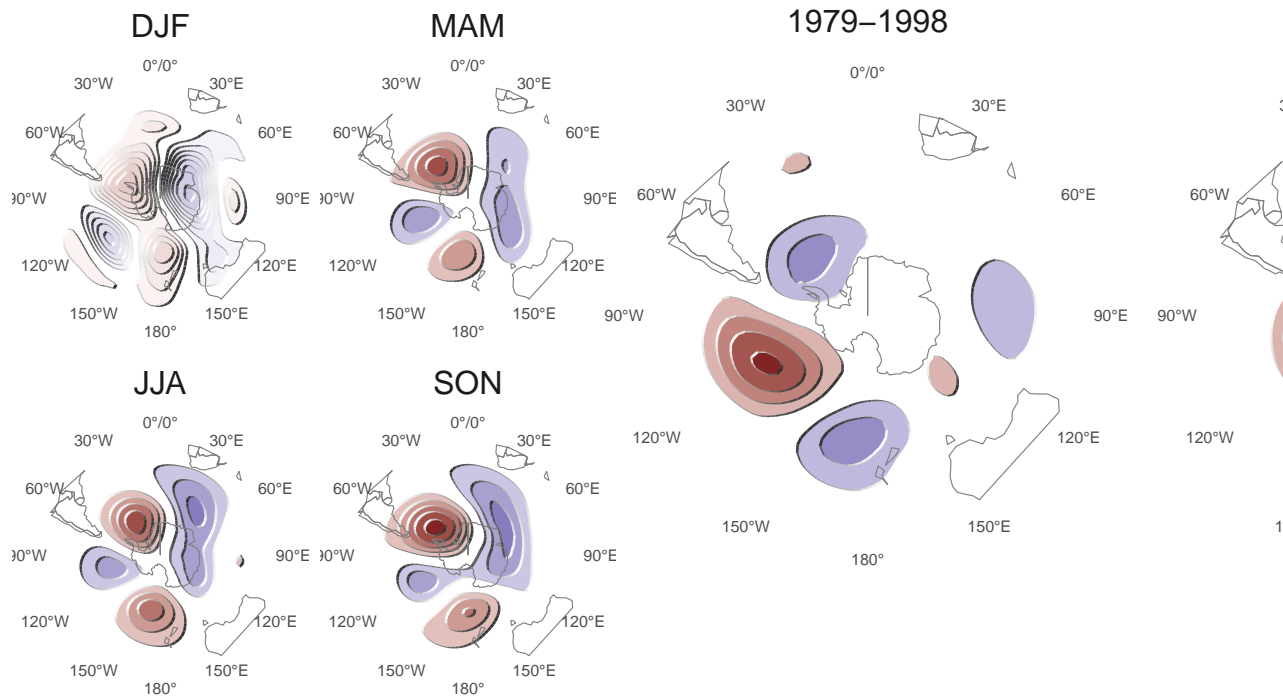


FIG. A6: Zonal of projection of 700 hPa onto the first EOF of each season.

fig:A10

FIG. A7: Spatial patterns of the first EOF of 700 hPa geopotential height computed for the periods 1979 to 1998 and 1999 to 2018. Full field (left), zonally asymmetric component (middle) and zonally symmetric component (right). Pattern correlation between both fields is 0.77. Arbitrary units.

fig:A11